Cu_2ZnSnS_4, a Fascinating Counter Electrode for TiO_2-Free Dye-Sensitized Solar Cells

Anurag Roy,*[a] and Senthilarasu Sundaram[a], Tapas K. Mallick[a]

[a] Environment and Sustainability Institute, University of Exeter, Penryn Campus, Cornwall TR10 9FE, United Kingdom
Email: A.Roy30@exeter.ac.uk

Abstract: Since innovation, different dye-sensitized solar cells (DSSCs) have endeavored with additional components to escalate the efficiency, cost-effectiveness and long-term stability. Various approaches have been executed to reduce the amount of costly platinum (Pt) used in DSSCs and/or to explore cheaper alternatives to Pt. In this work, cheaper elements based quaternary chalcogenide alloy; Cu_2ZnSnS_4 (CZTS) has been projected as a prominent counter electrode (CE) candidate to Pt in DSSCs. The CZTS thin film has been developed by an *in-situ* synthesis employing a hydrothermal technique and further evaluating various physicochemical characterization. Our results manifest that using the CZTS CE, a power conversion efficiency (PCE) of 4.3% was exhibited for TiO_2 based photoanode. The highest PCE of 6.5% was achieved for $BaSnO_3$ based photoanode, a promising alternative oxide to TiO_2 photoanode. This work further signifies a unique combination of newly developed $BaSnO_3$(BSO)-CZTS DSSCs, could be a promising competitor to TiO_2-Pt DSSCs.

Introduction

Third-generation photovoltaics are considered for their low-cost, convenient and straightforward approaches, aiming to circumvent the Shockley-Queisser limit to achieve better power conversion efficiency (PCE) compared to the other photovoltaics. [1] However, the technological challenge is to utilize the full solar spectrum by using new materials to achieve the maximum PCE. Dye-sensitized solar cells (DSSCs) appear as a reliable alternative among other photovoltaic devices consists of a simple photoelectrochemical device set up using low-cost materials. [2] A DSSC is, in essence, a photochemical cell which contains two electrodes and an electrolyte and generates electrical current by redox reactions. The TiO_2 and Pt are considered the best-suited device material to exhibit higher PCE and set up a traditional device set-up using those materials in DSSC. [2,3] In order to enhance the performance and find out a suitable alternative, significant efforts have been accomplished in improving the TiO_2-Pt, which acts as a framework for DSSCs. Among the current challenges, this work has been focused on developing new materials, which are alternative to Pt, and their associated more reliable alternative to TiO_2 with the modified synthesis technique and improved physicochemical properties to achieve enhanced efficiency.

The counter electrode (CE) holds a significant performance-evaluating component in DSSC in accepting the free electron from the external circuit, hole recovery, and catalyzing the liquid electrolyte reduction. Pt stands out as an excellent CE material and sets a benchmark for DSSC. [4] The electronic band alignment relationship between Pt and redox electrolyte put together Pt as an ideal CE. This connection must be appraised in the process of developing new CE catalysts and other new redox couples.
The introduction of new materials and device developments can significantly increase the conventional DSSC device's regular performance.

The issue with Pt-based CE lies on its cost and gets corroded in the liquid electrolyte presence. In this regards, finding and developing an alternative to substitute Pt with all its salient features is a significant challenge and huge demand. [5] However, extensive efforts have been executed to implement less expensive and naturally abundant materials as the Pt-free catalyst in DSSCs. [6,7] Compared to Pt, the CEs of transition metal oxides, sulfides, nitrides, and carbides exhibited promising electrocatalytic performance in DSSCs. As a promising non-Pt based CEs, inorganic compound in the form of alloys, oxides, nitrides, carbides, and sulfide, conducting polymers, and various carbonaceous materials are extensively studied. [8-10]
In particular, sulfide-based CEs have the eminence in facile preparation, better chemical stability, and excellent electrocatalytic property compared to the other alternative CEs. [11-13] Recently, using naturally abundant element derived a quaternary semiconductor Cu_2ZnSnS_4 (CZTS) is withdrawn much attention due to its superior p-type electrochemical properties such as high-hole concentration (~$1.2x10^{15}$ - $3.1x10^{20}$ cm^{-3}). [14-17] CZTS solar cells have shown a remarkable improvement in performance, reaching 12.6% power conversion efficiency (PCE). Despite, CZTS as a light absorber layer for thin-film solar cells, this may emphasis a major electrochemical catalyst for DSSCs.
However, impurity counterparts like Cu_2S, ZnS, SnS, SnS_2, and Cu_2SnS_3 interfere with achieving a high PCE CZTS CE, impeding photoelectrochemical properties of CZTS. [18, 19] Consisting complexity multications, there is a relative scope to introduce the counterpart's phases. Impurity free CZTS consists of a direct bandgap (E_g) in ~1.4-1.5 eV. Besides, a high absorption coefficient >10^4 cm^{-1} along with intrinsic p-type conductivity belongs to CZTS.[16, 20,21]These remarkable merits facilitate faster hole mobility and recovery, leading to improved device performance.
CZTS has been already implemented as a commendable surrogate candidate to Pt-based CE for DSSCs. Guo et al. (2010) has developed CZTSSe film by a simple process of the spin-coating method and achieved a power conversion efficiency (PCE) of 7.2%.[22] Besides, CZTSSe nanocrystals were further synthesized by Xin et al. (2011), which exhibits the highest PCE of 7.37%, resulting in a promising performance as a suitable alternative to Pt. [23] Sawant et al. (2020) recently developed CZTS CE for various morphology tuned TiO_2 photoanode in DSSCs. The highest efficiency measured was 2.65% for micro-flower like TiO_2 structures with CZTS photoanode. [24] Besides, surfactant mediated TiO_2 device reveals 6.24% PCE for hydrothermally synthesized CZTS, as reported by the same group. [25] Chen et al. (2014) employed a convenient solution method and a rapid heating process to prepare a well crystalline, high surface area CZTSSe CE, resulted in 7.4% of PCE. [26] Mary et al. (2020) also report that CZTS nanoflakes as CE showed the PCE of 2.95%, comparable to the DSSC with Pt (3.11%).[27] Electrocatalytic activity of CZTS/graphene counter electrode was evaluated by Wei et al. (2020), where the authors demonstrated the catalytic activity and conductivity using a varied weight ratio of graphene in the composited material of CZTS/graphene to make a CE, showing the highest PCE of 3.71%.[28] A series of quaternary chalcopyrite sulfide semiconductors Cu_2MSnS_4 (M = Zn, Ni, Co, Mn, Fe) was developed by Baskaran et al. (2020) and evaluated their performance in DSSC. [29]

Despite that, the morphology of CZTS plays a crucial role to control its performance for a DSSC device. Variation of CZTS nanostructures can further improve the PCE. [30, 31] In this work, we find more inexpensive CZTS can be a suitable alternative to costly Pt, which has been developed starting from CZTS thin film preparation, its various physicochemical characteristics and finally explored as a non-Pt CEs for DSSCs. To overcome the drawback of binary oxides such as dye-metal oxide complex formation at low pH, degraded stability in acidic dye solutions, a prolonged period of dye loading, the idea of introducing ternary oxides as photoanodes were explored. As an emerging ternary oxide, $BaSnO_3$ (BSO), as photoanodes, has been studied to address the mentioned problems of TiO_2. [32] Consisting of high electron mobility, faster dye absorption rate, n-type resistivity, and low visible absorption, BSO becomes a promising alternative photoanode material for DSSC. [33] CZTS CEs exhibit better PCE with BSO compared to TiO2 and even better than Pt.

The synthesis of CZTS thin film has been espoused from the literature. [34] Details of CZTS synthesis has been described in the supporting information section. A digital photograph of as-prepared CZTS thin-film as deposited by the hydrothermal method has been given in Figure S1.

Results and Discussion

CZTS exhibits the thermodynamically lowest energy structure kesterite (space group I4), originated from the ternary chalcopyrite lattice framework, as shown in Figure 1a. Although, stannite structure can be secured at high-energy states due to the disorder in the Cu-Zn sub-lattice, as shown in Figure 1b. [16]

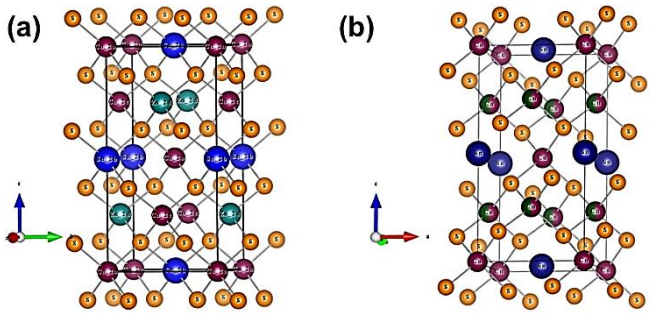

Figure 1. (a) Kestertite, (b) Stannite lattice framework of CZTS, as derived using VESTA. (Yellow: Sulphur; Burgundy: Copper; Blue: Tin; Green: Zinc)

Equations (1)-(4) indicate the possible CZTS phase formation, derived from their individual metal sulfide formation.

$$CuCl_2 \cdot 2H_2O + CH_4N_2S \xrightarrow{\Delta} CuS + 2HCl + 2NH_3 + CO_2 \quad (1)$$

$$ZnCl_2 + CH_4N_2S + 2H_2O \xrightarrow{\Delta} ZnS + 2HCl + 2NH_3 + CO_2 \quad (2)$$

$$SnCl_2 + 2CH_4N_2S + 2H_2O \xrightarrow{\Delta} SnS_2 + 2HCl + 2NH_3 + CO_2 \quad (3)$$

$$2CuS\,(s) + ZnS(s) + SnS\,(s) \xrightarrow{\Delta} Cu_2ZnSnS_4 \quad (4)$$

Continuous equilibrium maintenance of equation (4) initially leads to form Cu_2SnS_3 followed by a lattice rearrangement to Wurtzite and finally kesterite structure with the inclusion of Zn. It is noticeable that among the various secondary phases, the existence of SnS_2 on the surface of CZTS films is incurable for device performance, which will deplete the open-circuit voltage (V_{OC}) of the device. In this regard, thiourea, (CH_4N_2S) has been considered a sulfur source and feasible etchant for removing excess SnS_2. [18, 19] The X-ray diffraction (XRD) pattern of the as-deposited CZTS thin film is shown in Figure 2a. The major XRD peaks appear at 2θ = 28.38, 47.51 and 56.37° assigned to (112), (220) and (312) planes of stoichiometric kesterite structure and corroborate with the reference JCPDS file no. 26-0575. As mentioned earlier, there is a possibility to form the secondary phases such as $Cu_{2-x}S$, ZnS and SnS_2, Cu_2SnS_3, and the CZTS phase during the synthesis and annealing treatment. [16] The XRD result does not exhibit any of those secondary phases. In particular, the diffraction pattern of CZTS is indistinguishable from that of Cu_2SnS_3 with a cubic structure and ZnS with a zinc blende structure. However, to further confirm the pure phase of CZTS formation, Raman spectroscopy has been performed with the CZTS thin film, as given in Figure 2b. The intense characteristic peak at 284, 327 and 617 cm^{-1}, which is the characteristic peak of CZTS. Besides, the Raman spectrum does not exhibit any peak at 476 cm^{-1}, and 353 cm^{-1}, which is considered the distinct peaks of $Cu_{2-X}S$, and ZnS, respectively. [35] Therefore, the XRD and Raman analysis thus signify pure phase growth of CZTS thin film during the hydrothermal process. A typical Fourier-transform infrared (FTIR) spectrum of the CZTS powder is shown in Figure 2c. Various bands appeared at 500-2000 cm^{-1} represent multiple vibrational modes of M-M and M-S bonds where M= Cu, Zn and Sn. Simultaneously, the sample contains labile hydroxide (-OH) group at the surface arising out of hydrothermal synthesis. The UV-Vis absorption result, as shown in Figure 2d exhibits a broad spectrum with an ascending absorption at 800 to 400 nm with a maximum adsorption at ~500 nm. [36, 37] The zeta potential measurement, Brunauer-Emmett-Teller (BET) surface area and Barrett-Joyner-Halenda (BJH) pore size distribution of the same sample was also executed to understand the surface characteristics of the synthesized CZTS and the corresponding results are tabulated in Table 1.

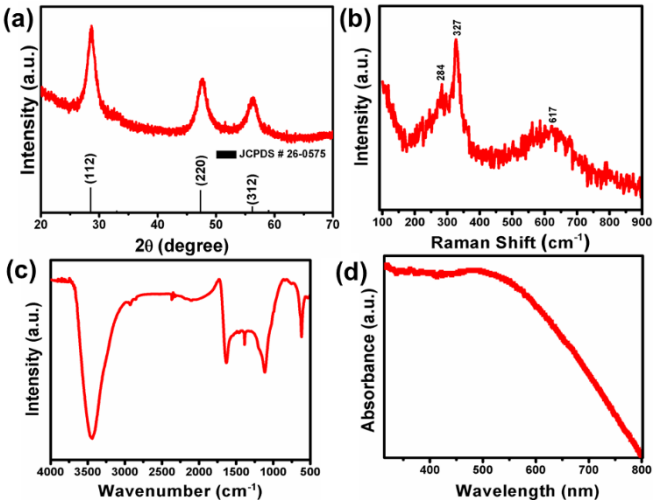

Figure 2. (a) X-ray diffraction pattern of Cu_2ZnSnS_4 along with the standard pattern of Cu_2ZnSnS_4 (JCPDS No. 26-0575), (b) Raman, (c) FTIR and (d) UV-Vis absorption spectrum of hydrothermal synthesized CZTS sample.

It is evident from the transmission electron microscopy (TEM) images that hydrothermally synthesized CZTS adopts particle-like

shape, as shown in Figure 3a and 3b. The average crystalline size was calculated as ~22 nm from the histogram given in Figure S2. Corresponding, high-resolution TEM (HRTEM) image, as shown in Figure 3c, confirms the single-crystalline lattice fringes for kesterite-structure of CZTS (112) reflection having an interlayer spacing of 0.31. Inset shows the corresponding fast Fourier transform (FFT) image of the HRTEM in particular. The corresponding SAED pattern in Figure 3d has been indexed to the (112), (220) and (312) planes of CZTS. No apparent additional sulfide phases are observed, and the pure phase of the CZTS film is further confirmed from the above observation. The energy-dispersive X-ray (EDX) elemental signals obtained by TEM analsyis also reflect the presence of Cu, Zn, Sn and S as the only elements of the sample shown Figure S3.

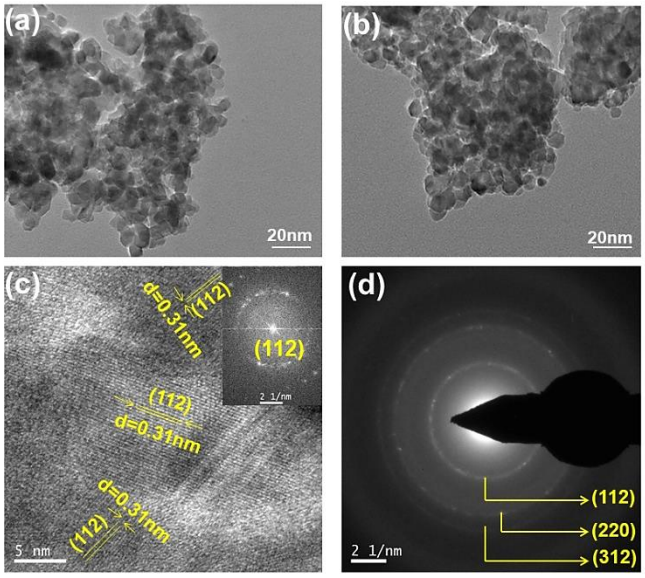

Figure 3. (a), (b) TEM bright-field image of CZTS nanoparticles, (c) corresponding HRTEM image (inset: corresponding FFT pattern) and (d) SAED pattern of CZTS nanoparticles, respectively.

Table 1. Comparative parameters of various characterizations for CZTS nanoparticles.

Zeta Potential (mV)	Electrophoric Mobility at 300 K x 10^{-3} (cm^2/Vs)	BET surface area (m^2/g)	BJH pore size (nm)
-22.2	0.128	35	5-8

In CZTS, it is imperative to deal with the correct phase and elemental distribution during the synthesis and its application. Phase control and growth are crucial, which has a severe impact on photovoltaic performance. The energy-dispersive X-ray spectroscopy (EDX) colour mapping elemental analysis has been performed with the synthesized CZTS nanoparticles to identify the same, as shown in Figure 4. The result further illustrates the homogeneous distribution of Cu (Green), Zn (Purple), Sn (Indigo) and S (Red) as the only elements over a wide range of area (10 µm) with atomic (%) of 26.73, 10.85, 13.64 and 48.78 bearing a ratio of 0.27:0.11:0.14:0.49, respectively, indicating Cu_2ZnSnS_4 alloy formation, and the corresponding spectrum is shown in Figure S4.

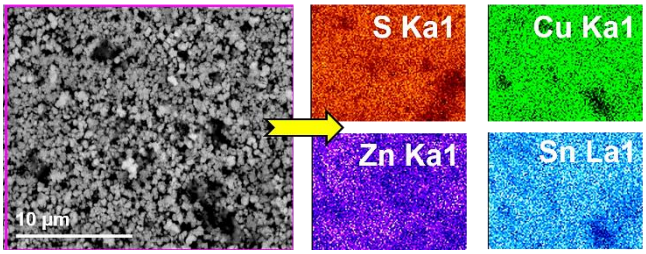

Figure 4. Elemental colour mapping images of CZTS nanoparticles.

The field emission scanning electron microscope (FESEM) microstructural image shown in Figure S5a exhibits an overview of the morphology of the hydrothermally grown homogeneous CZTS film on FTO. A thickness of ~500 nm was measured from its corresponding cross-sectional FESEM image shown in Figure S5b.

On the other hand, TiO_2 emphasises as a standard photoanode framework for DSSCs. Desirable electronic band alignment from most popular dyes, high surface area, a robust, stable, ideal scaffold for dye anchoring and high electron mobility for photo-generated electron collection establishes TiO_2 (E_g ~3.2 eV) as the most suitable, photoanode in DSSC. However, dye complexation, dye loading time, inferior free-electron lifetime, and almost saturated PCE etc. could be some of the disadvantages of TiO_2. Thus there is a requirement of an alternative to TiO_2. Recently, a simplified ternary oxide, BSO envisages as a suitable alternative to TiO_2. BSO is a critical n-type semiconductor (E_g ~3.1 eV) with a perovskite structure that has drawn much attention due to its higher electron mobility and faster dye sensitizing capability at room temperature the traditional binary oxides, TiO_2 and ZnO.

Figure 5a and Figure 5b manifests TEM bright-field and HRTEM images of commercial TiO_2 paste used as a photoanode for this study, respectively. The anatase TiO_2 nanoplates exhibit highly crystalline, well-defined morphology. The FESEM microstructural image of the corresponding photoanode is represented in Figure 5c. The synthesized BSO shows porous nanostructured morphology, as shown in its TEM bright-field image in Figure 5d. The corresponding HRTEM image of porous BSO nanoparticles excels cubic perovskite phase, as shown in Figure 5e. Figure 5f represents FESEM image of BSO-based photoanode. The TiO_2 and BSO-based photoanodes were developed by three-layer deposition of the screen printing method, consisting of an average thickness of 9.2 ± 0.5 µm. BSO consists of faster dye loading time (1 h) compared to TiO_2 (24 h), which is precedence to prospect BSO as a suitable alternative to TiO_2. [32]

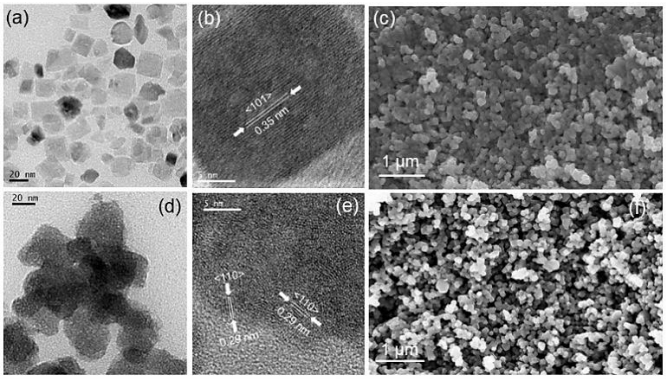

Figure 5. (a) TEM bright field image of TiO_2 nanoparticles, (b) coressponding HRTEM image (scale bar 5 nm), (c) FESEM microstructural image of screen-printed TiO_2 film, (d) TEM bright-field image of BSO nanoparticles, (e) corresponding HRTEM image (scale bar 5 nm) and (f) FESEM microstructural image of screen printed BSO film.

Further, the synthesized CZTS CE catalytic activity is tested by cyclic voltammetry (CV) analysis with the I^-/I_3^- electrolyte and Ag/AgCl as a reference electrode, as shown in Figure 6. CZTS-1 indicates as prepared film, CZTS-2 indicates film curing at 80ºC for two days. On the other hand, CZTS-3 is the third day of CZTS-1 film, and similarly, CZTS-4 is the second day of CZTS-2 film. This work's intension lies in understanding the electrochemical behaviour of CZTS film compared to Pt for different days. The notable CV voltammogram observed at a negative potential region -0.34 V vs Ag/AgCl of CZTS 1 electrode demonstrates the trioxide reduction's catalytic activity. [38] The result indicates CZTS 1 exhibits the highest catalytic activity and comparable to Pt, and hence selected for DSSC testing.

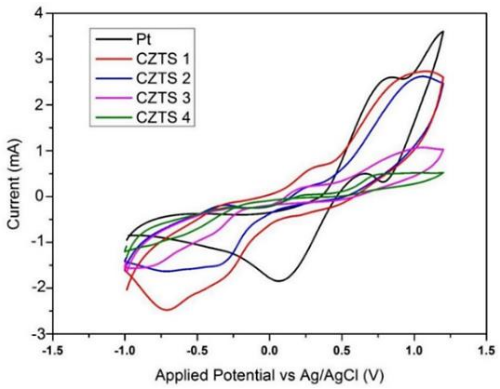

Figure 6. Cyclic voltammogram of CZTS thin film compared to Pt for a three-electrode system with the I^-/I_3^- electrolyte.

The comparative photovoltaic performance as *J-V* characteristics plot is shown in Figure 7, and corresponding parameters for each of them have been further illustrated in Table 2. The fabricated CZTS exhibited a maximum PCE of 4.31 % with a short circuit current (J_{SC}) 6.84 mA.cm^{-2}, open-circuit voltage (V_{OC}) 0.74 V and a fill factor (FF) of 0.54 for TiO_2 based photoanode. On the contrary, the CZTS counter electrode exhibited the highest PCE of 6.65 % with a J_{SC} 15.94 mA.cm^{-2}, V_{OC} 0.72 V and FF of 0.51, for BSO-based photoanode. The *J-V* characteristics evaluate the BSO based device exhibit higher efficiency than the TiO_2 based devices for CZTS counter electrode. It is noteworthy that the J_{SC} value is quite lower (6.84 mA.cm^{-2}) for TiO_2-based Photoanode, whereas BSO-based Photoanode exhibits more than double time J_{SC} (15.94 mA.cm^{-2}). The results are quite interesting and signify BSO favours freer electron than TiO_2 for CZTS CE. Besides, the photovoltaic performance of CZTS CE is also comparable with the Pt CE. Table 2 manifests Pt resulted in better PCE in case of TiO_2 based photoanode, whereas CZTS is functioning well for BSO based photoanode. The exciting fact is here to be noted that both the CZTS-based devices exhibit a V_{OC} of > 0.7 V for both types of photoanodes. However, CZTS CEs are abdicated lower FF for both types of photoanodes.

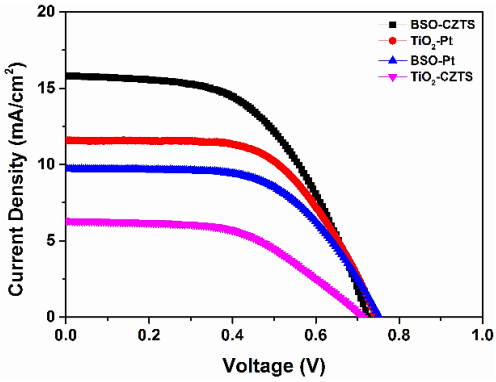

Figure 7. *J-V* plot of DSSC fabricated with different photoanode materials (TiO_2 and BSO) with counter electrodes (CZTS and Pt).

Table 2. Photovoltaic performance of CZTS CE for TiO_2 and BSO-based photoanodes in DSSCs.

Cell	J_{SC} (mA.cm^{-2})	V_{OC} (V)	FF	PCE±0.1 (%)
TiO_2-Pt	11.55	0.74	0.59	5.42
TiO_2-CZTS	6.84	0.72	0.54	4.31
BSO-Pt	8.87	0.75	0.60	4.51
BSO-CZTS	15.94	0.72	0.51	6.52

EIS studies (Nyquist plot) were performed on the same devices of BSO-CZTS and TiO_2-Pt to understand the transport properties at different interfaces in the DSSC assembly, as shown in Figure 8a. The frequency range selected for the measurement was 10^{-2} Hz to 10^6 Hz with an alternating current (AC) amplitude of 10 mV. As the electrolyte used is the same for all cases, the interface of our interest for the sake of comparison is the BSO-CZTS, and TiO_2-Pt electron transport properties originated from their respective interfaces. BSO-CZTS device exhibits lowest charge transfer resistance (R_{CT}) value as 32.81 ohm.cm^{-2} than TiO_2-Pt device for which The R_{CT} value is 35.65 ohm.cm^{-2}, respectively. Interestingly, the series resistance (R_S) values are almost similar for both the devices, nearly ~17.51 ohm.cm^{-2}. Both the devices reduce charge diffusion towards the electrolyte at high frequencies a side arc and a most right-handed peak are distinguishable among the rest devices. The EIS parameters significantly affect the FF and J_{SC} of the DSSCs. The Bode phase plots (Figure 8b) display the charge transfer process's frequency peaks and evaluate the electron lifetimes for the BSO-CZTS and TiO_2-Pt devices. The peak frequency of the central arc describes the rate of recombination of electrons in the film. The estimated lifetime indicates BSO-CZTS device exhibits longer electron lifetime of 3.45 ms, whereas the shortest lifetime recorded for TiO_2-Pt device is 0.15 ms.

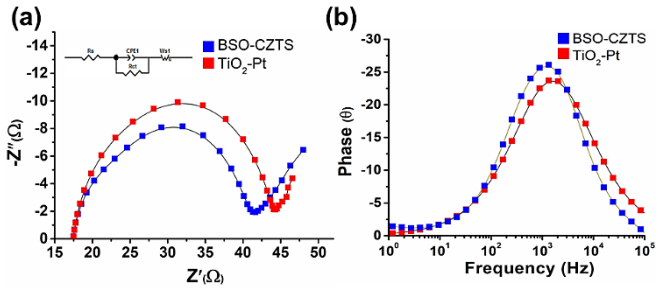

Figure 8. (a) Nyquist plot, and (b) corresponding Bode plot for BSO-CZTS and TiO_2-Pt devices, respectively.

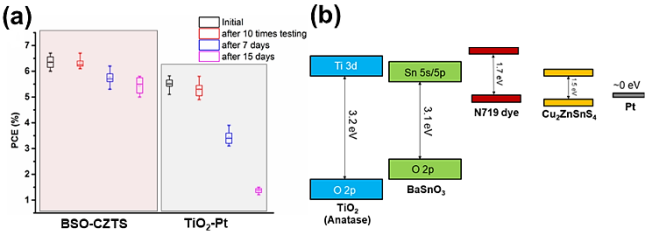

Figure 9. (a) Error bar plot for BSO-CZTS and TiO_2-Pt devices in terms of their corresponding efficiency for the different set of periods, (b) schematic representation of the band alignment of CZTS-based DSSC components.

To further understand the sufficient stability of the CZTS-based DSSCs for both devices, we have also investigated the performance stability of the BSO-CZTS devices, and compared with TiO_2-CZTS devices shown in Figure 9a. The electrolyte is the same for both the devices, i.e. I^-/I_3^- electrolyte. We have monitored the effect of photoanode-CE pairing for their long-term performance and measured up to 15 days through this analysis. Figure 9a shows an error bar plot of recorded PCE as achieved for both the devices in different periods. The TiO2-Pt devices' efficiency was drastically depleted, whereas there is a steady reduction in PCE was observed in the case of BSO-CZTS devices. This result indicates that CZTS CE's stability is comparatively superior with the BSO compared to TiO_2, it can be suitable for BSO-based device, as a promising alternative to TiO_2. An overall PCE decrement is causing due to corrosive liquid I^-/I_3^- electrolyte at ambient. To understand the effect of corrosive liquid I^-/I_3^- electrolyte on the CZTS, we have consecutively measured XRD of the CE films for a different time, as shown in Figure S6. The resulting data signifies CZTS is relatively stable towards the corrosive liquid I^-/I_3^- electrolyte and avoids any oxidation tendency like Pt. Different stability measurements all suggested that the BSO-CZTS devices possessed better stability toward the iodide electrolyte than TiO_2-Pt CE.

Figure 9b illustrates the electronic bandgap alignment diagram of BSO and TiO_2, along with the N719 dye, CZTS and Pt. In terms of the bandgap alignment, the conduction band (CB) of BSO places in a higher position than the CB of TiO2 and brings closure to the HOMO (highest energy occupied molecular orbital) of the N719 dye molecule.[39] Possessing a small effective mass and high electron mobility further escalate BSO towards a highly dispersed band structure.[40] This facilitates rapid electron diffusion, which can effectively contribute to the higher PCE generation. It is anticipated that the band alignment and interface properties, as shown in Figure 9b furnishes an optimistic approach for designing higher efficiency CZTS-based solar cells. Besides, due to the higher the cathodic peak current density, CZTS expresses the almost similar catalytic activity as a CE compared to Pt. [41] Besides, inhomogeneous metal-dye complex formation on the surface commutes the surface properties from comparatively hydrophobic to hydrophilic nature and degrades performance. [42] BSO-based photoanode is relatively stable to this type of acidic dyes and does not allow any dye blockage, leading to the device's stability. Besides, the CZTS network provides sufficient large active catalytic area for I_3^- reduction, which further facilitates the electron transfer. The high-energy (112) facets of CZTS have remarkable reducibility for I_3^- ions, enhancing the photoelectrochemical activity followed by high carrier concentration and low resistivity, which can accelerate the transportation of photo-generated electron at the electrode/redox electrolyte interface. [43]

Table 3 highlights some significant performance of CZTS-based CEs in DSSCs. The results obtained in this work are quite competitive and exciting compared to the others report and can be appraised as an alternative to Pt.

Table 3. Comparative photovoltaic performances of various CZTS-based CEs in DSSCs.

Description	J_{SC} ($mA.cm^{-2}$)	V_{OC} (V)	FF (%)	Champion PCE (%)	Ref.
In-situ grown CZTS with different thickness	12.45	0.72	63	5.56	14
Morphology varied TiO_2	9.2	0.46	61	2.65	24
Surfactant mediated TiO_2	13.25	0.76	61	6.24	25
Two-dimensional CZTS	21.78	0.78	51	8.67	44
Graphene added CZTS	16.77	0.71	66	7.81	45
[Cu]/[Zn] + [Sn] molar ratio in the CZTS	17.20	0.74	62	7.94	46
First time with $BaSnO_3$-based photoanode	15.94	0.72	0.51	6.52	This Work

Element substitution of kesterite CZTS also shows a feasible solution to achieve higher efficiency. Substitution of Zn^{2+} with Co^{2+}, and Ni^{2+} leads to form Cu_2CoSnS_4 and Cu_2NiSnS_4, which exhibits >8% PCE for a DSSCs.[47] WO_3 modified $Cu_2ZnNiSe_4$, another quaternary CE was further employed, which attained a PCE of 12.16%.[48] Besides, $(Cu_{1-x}Ag_x)_2ZnSnS_4$ nanoparticles attained the E_g in the range of 1.43-1.64 eV, which is quite impressive to use as low-cost CE. Most of the DSSCs are engaged with the TiO_2-based Photoanode and related framework.[49]

Interestingly, all these studies portraits a massive possibility of the element substitution method without changing the material's structure effectively improved potential catalysts performance and could effectively boost the PCE for a BSO-based photoanode in the future. The estimated band gaps from the absorption

spectrum and electrochemical CV measurements range from 2.5-1.8 eV. They also exhibit strong absorption in the visible region, stipulating their suitability as active absorber layer material for solar cells. Hence, it is expected that the CZTS with appropriate band structure configuration, geometrical morphology and photoelectrochemical stability may turn out to be a novel material for the photovoltaic research. Our study further paves the way about the future development of alternative materials for a new set of DSSC.

Conclusion

Pt-free efficient hydrothermally developed *in-situ* CZTS counter electrode (CE) was fabricated. The fabricated film was further characterized using various physicochemical characterization techniques. The XRD and Raman analysis revealed that the developed CZTS film is free of its analogue impurity. Besides, TEM study shows an average particle size of the synthesized CZTS ~22 nm. Finally, the CZTS CEs were employed for DSSC testing. Significant results of CZTS as CE material were further extracted with TiO_2 and one of its major leading alternative photoanode such as $BaSnO_3$ (BSO). The TiO_2-based device exhibits the highest efficiency of 4.31% whereas BSO-based device shows the highest efficiency of 6.52%.

Interestingly, for both the cases, the open-circuit voltage and fill factor remains almost similar; however, there is a significant enhancement of short-circuit current density was observed in the case of BSO. The photovoltaic performances further signify a more reliable charge carrier transport interface with BSO compared to TiO_2 with the CZTS-based CE. All these advantages accelerate the performance progress of DSSCs. In this way, this work creates a new window for BSO-CZTS based DSSCs, which is an effective alternative to TiO_2-Pt-based DSSCs and can pave the way a futuristic new material framework for DSSCs. However, the DSSC performance of CZTS CEs can exhibit a significant undertaking and more efficiency on proper modification and optimization of the fabrication process and thin-film development. The encouraging result of this work on DSSC unfolds a fascinating way to achieve maximum PCE and improved performance.

Supporting Information Summary

Details of CZTS synthesis and DSSC device fabrication along with materials characterizations. Particle size histogram plot and EDX analysis of CZTS nanoparticle as obtained by TEM analysis. Quantitative EDX spectrum of CZTS thin film. FESEM microstructural images of hydrothermally grown CZTS film, XRD pattern of CZTS thin film for the different set of periods are included in the corresponding supporting information file,

Acknowledgements

A.R. gratefully acknowledges CSIR-Central Glass and Ceramic Research Institute, Kolkata 700032, India, supporting material characterization. A.R. also acknowledges Newton-Bhabha PhD Placement Program 2016-2017. Authors also thankful to College of Engineering, Mathematics and Physical Sciences, University of Exeter.

Conflict of Interest

The authors declare no conflict of interest.

Keywords: Alloys • Counter Electrode • Dye-sensitized Solar Cell • Materials Science • Platinium Free

[1] G-R. Li, X-P. Gao, *Adv. Mater.* **2020**, *32*, 1806478.
[2] N. Mariotti, M. Bonomo, L. Fagiolari, N. Barbero, C. Gerbaldi, F. Bella, C. Barolo, *Green Chem.* **2020**, *22*, 7168-7218.
[3] M.C. Beard, J.M. Luther, A.J. Nozik, *Nat. Nanotechnol.* **2014**, *9*, 951-954.
[4] J. Gong, K. Sumathy, Q. Qiao, Z. Zhou, *Renew. Sust. Energ. Rev.* **2017**, *68(1)*, 234-246.
[5] J. Briscoe, S. Dunn, *Adv. Mater.* **2016**, *28*, 3802-3813.
[6] M. Wu, X. Lin, Y. Wang, L. Wang, W. Guo, D. Qi, X. Peng, A. Hagfeldt, M. Grätzel, T. Ma, *J. Am. Chem. Soc.* **2012**, *134*, 3419-3428.
[7] S. Yun, P. D. Lund, A. Hinsch, *Energy Environ. Sci.* **2015**, *8*, 3495-3514.
[8] M. R. Samantaray, A.K. Mondal, G. Murugadoss, S. Pitchaimuthu, S. Das, R. Bahru, M.A. Mohamed, *Materials* **2020**, *13*, 2779.
[9] U. Ahmed, M. Alizadeh, N. A. Rahim, S. Shahabuddin, M. S. Ahmed, A.K. Pandey, *Sol. Energy* **2018**, *174*, 1097-1125.
[10] J. Theerthagiri, A.R. Senthil, J. Madhavan, T. Maiyalagan, *Chem. Electro. Chem.* **2015**, *2*, 928 -945.
[11] Z. Shi, K. Deng, L. Li, *Sci. Rep.* **2015**, *5*, 9317.
[12] J. Xu, H. Xue, X. Yang, H. Wei, W. Li, Z. Li, W. Zhang, C.S. Lee, *Small* **2014**, *10*, 4754-4759.
[13] C.Y. Yang, C.W. Chen, C.L. Liu, H.T. Li, *Adv. Energy Mater.* **2011**, *1*, 259-264.
[14] S. Chen, A. Xu, J. Tao, H. Tao, Y. Shen, L. Zhu, J. Jiang, T. Wang, L. Pan, *ACS Sustain.Chem.Eng.* **2015**, *3*, 2652-2659.
[15] S. Chen, J. Tao, H. Tao, Y. Shen, L. Zhu, J. Jiang, X. Zeng, T. Wang, *Mater. Technol.* **2015**, *30*, 306-312.
[16] A. Roy, P.S. Devi, S. Karazhanov, D. Mamedov, T.K. Mallick, S. Sundaram, *AIP Adv.* **2018**, *8*, 070701.
[17] S. Chen, A. Walsh, X.-G. Gong, S.-H. Wei, *Adv. Mater.* **2013**, *25*, 1522-1539.
[18] E. Indubalaa, S. Sarveshvaran, V. Sudha, A. Y. Mamajiwala, S. Harinipriya, *Sol. Energy* **2018**, *173*, 215-224.
[19] W. Wang, G. Chen, H. Cai, B. Chen, L. Yao, M. Yang, S. Chen, Z. Huang, *J. Mater. Chem. A* **2018**, *6*, 2995-3004.
[20] H. Matsushita, T. Ichikawa, A. Katsui, *J. Mater. Sci.* **2005**, *40*, 2003.
[21] C. Wang, S. Chen, J.-H. Yang, L. Lang, H.-J. Xiang, X.-G. Gong, A. Walsh, S.-H. Wei, *Chem. Mater.* **2014**, *26*, 3411-3417.
[22] Q. Guo, G. M. Ford, W.-C. Yang, B. C. Walker, E. A. Stach, H.W. Hillhouse, R. Agrawal, *J. Am. Chem. Soc.* **2010**, *132*, 17384-17386.
[23] X. Xin, M. He, W. Han, J. Jung, Z. Lin, *Angew. Chem. Int. Ed.* **2011**, *50*, 11739 -11742.
[24] J. P. Sawant, R.B. Kale, *J. Solid State Electrochem.* **2020**, *462* (24), 461-472.
[25] J. P. Sawant, R.B. Kale, *Mat. Lett.* **2020**, *265*, 127407.
[26] H. Chen, D. Kou, Z. Chang, W. Zhou, Z. Zhou, S. Wu, *ACS Appl. Mater. Interfaces* **2014**, *6*, 20664-20669.
[27] C. I. Mary, M. Senthilkumar, G. Manobalaji, S. M. Babu, *J. Mater. Sci: Mater. Electron.* **2020**, *31*, 18164-18174.
[28] L. Wei, Q. Wu, W. Chen, D. Wang, B. Jiang, G. Sun, F. Yu, J. Feng, Y. Yang, *J. Solid State Electrochem.* **2020**, *24*, 263-272.
[29] P. Baskaran, K. D. Nisha, S. Harish, S. Prabakaran, M. Navaneethan, J. Archana, S. Ponnusamy, C. Muthamizhchelvan, H. Ikeda, *J. Mater. Sci.* **2021**, *56*, 4135-4150.
[30] A.S. Nazligul, M. Wang, K.L. Choy, *Sustainability* **2020**, *12*, 5138.
[31] Y. Xie, C. Zhang, F. Yue, Y. Zhang, Y. Shi, T. Ma, *RSC Adv.*, **2013**,*3*, 23264-23268.
[32] A. Roy, P.P. Das, P. Selvaraj, S. Sundaram, P.S. Devi, *ACS Sustainable Chem. Eng.* **2018**, *6*, 3299-3310.
[33] A. Roy, P. Selvaraj, P.S. Devi, S. Sundaram, *Mat. Lett.* **2018**, *219*, 166-169.
[34] Z. Yan, A. Wei, Y. Zhao, J. Liu, X. Chen, *Mater. Lett.* **2013**, *111(15)*, 120-122.
[35] Y. Havryliuk, M.Y. Valakh, V. Dzhagan, O. Greshchuk, V. Yukhymchuk, A. Raevskaya, O. Stroyuk, O. Selyshchev, N. Gaponik, D. R. T. Zahn, *RSC Adv.* **2018**,*8*, 30736-30746.
[36] J. Wang, P. Zhang, X. Songa, L. Gao, *RSC Adv.* **2014**, 4, 27805-27810.
[37] Y. Xia, Z. Chen, Z. Zhang, X. Fang, G. Liang, *Nanoscale Res. Lett.* **2014**, *9*, 208.

[38] D. David Kirubakaran, S. Pitchaimuthu, C. R. Dhas, P. Selvaraj, S. Zh. Karazhanov, S. Sundaram, *Mat. Lett.* **2018**, *220*, 122-125
[39] D.W. Kim, S.S. Shin, S. Lee, I.N. Cho, D. H. Kim, C. W. Lee, H. S. Jung, K.S.Hong, *Chem. Sus. Chem.* **2013**, *6*, 449-454.
[40] N. Rajamanickama, P. Soundarrajan, K. Jayakumara, K. Ramachandran, *Sol. Energy Mater. Sol. Cells* **2017**, *166*, 69-77.
[41] S. Gnanasekar, P. Kollu, S.K. Jeong, A. N. Grace, *Sci. Rep.* **2019**, *9*, 5177.
[42] K. Fan, J. Yu, W. Ho, *Mater. Horiz.* **2017**, *4*, 319-344.
[43] X. Zhang, Y. Xu, J. Zhang, S. Dong, L. Shen, A. Gupta, N. Bao, *Sci. Rep.* **2018**, *8*, 248.
[44] S.-L. Chen, A.-C. Xu, J. Tao, H.-J. Tao, Y.-Z. Shen, L.-M. Zhu, J.-J. Jiang, T. Wang, L. Pan, *Green Chem.* **2016**, *18*, 2793-2801.
[45] L. Baia, J. N. Ding, N. Y. Yuan, H. W. Hu, Y. Li, X. Fang, *Mater. Lett.* **2013**, *112*, 219-222.
[46] M. S. Fan, J. H. Chen, C. T. Li, K. W. Cheng, K. C. Ho, *J. Mater. Chem. A* **2015**, *3*, 562-569.
[47] S. Lu, H. Yang, F. Li, Y. Wang, S. Chen, G. Yang, Y. Liu, X. Zhang, *Sci. Rep.* **2018**, *8*, 8714.
[48] W.C. Oh, K.Y. Cho, C.H. Jung, Y. Areerob, *Sci. Rep.* **2020**, *10*, 4738.
[49] N. Liu, F. Xu, Y. Zhu, Y. Hu, G. Liu, L. Wu, K. Wu, S. Sun, F. Hong, *J Mater Sci: Mater. Electron.* **2020**, *31*, 5760-5768.

Entry for the Table of Contents

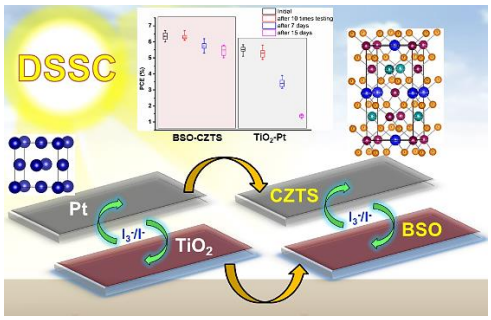

Investigation on the adequate performance of cheaper CZTS-based counter electrode for BSO-based DSSCs, explored as an effective alternative to costly Pt and TiO_2, respectively, which could elucidate more extended device performance compared to TiO_2-Pt-based DSSCs.

Supporting Information

Experimental Section

An *in-situ* fabrication technique using the hydrothermal method was successfully adopted to develop the CZTS thin film on an FTO coated glass. 2 cm x 2 cm sized FTO glasses were purchased from Sigma Aldrich, U.K. consisting a surface resistivity of ~7 Ω. sq^{-1}., and the transmittance of 82%. In a typical synthesis, 1 mmol of copper (II) chloride dihydrate ($CuCl_2$. $2H_2O$, Merck), 2 mM of zinc (II) chloride ($ZnCl_2$, Merck), 0.5 mmol of tin (II) chloride dihydrate ($SnCl_2.2H_2O$, Merck), 10 mmol of thiourea (CH_4N_2S, Merck) and 0.09 g hexadecyl trimethyl ammonium bromide (CTAB, Alfa Aesar) was dissolved, mixed and stirred in 3:1 solution mixture of 40 ml of water and ethanol in a 50 ml beaker and continuously stirred for 30 mins. Meantime, the FTO coated glasses were cleaned by sonication sequentially in a soap solution and distilled water and isopropanol for 15 mins. The cleaned glasses were then placed inside an ultraviolet ozone cleaner chamber (Ossila, UK) for 15 mins to remove contamination on the sample's surface. After that, the conducting side of a cleaned FTO glass was titled against the wall in a 60 ml Teflon liner autoclave chamber, and the precursor solution was slowly filled to it and allowed for a hydrothermal treatment at 180^oC for 24 h. After that, the autoclave was allowed to cool down to room temperature. The FTO substrate was then rinsed with de-ionized water and subsequently dried in the ambient. A reddish-brown layer on the FTO glass substrate indicates the deposition of CZTS layers, whereas the blank FTO on the left side contains a transparent surface. The CZTS deposited FTO employed as a counter electrode to replace Pt in the experiment. The nanoparticles were also synthesized in the same manner without using FTO substrate and collected after centrifugation at 10,000 rpm with repeatedly wash with water and ethanol and dried at 80^oC under an IR lamp.

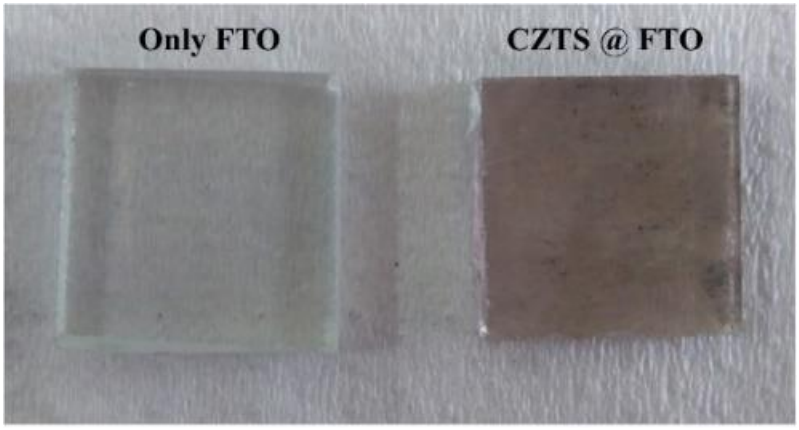

Figure S1. A photograph of the 2 cm x 2 cm (not in scale) FTO coated glass along with hydrothermal *in-situ* deposited CZTS on the FTO coated glass.

Materials Characterization

The XRD characterization was performed by BRUKER D8 Advance X-ray diffractometer (Cu Kα irradiation, 40 kV/40 mA, 0.02° 2θ step size). The Raman spectroscopic characterization was carried out on the STR500 (Cornes Technologies system using 514.5 nm Ar^+ green laser with 50 mW power). FTIR spectrum was measured using a Perkin Elmer, Spectrum Two FT-IR spectrometer between 4000 and 400 cm^{-1} wavenumbers. The fabricated carbon films' absorption spectra were measured on a UV-vis-NIR spectrophotometer (Shimadzu UV-3600). The synthesized powder morphology has been monitored on a Tecnai G2 30ST (FEI) high-resolution transmission electron microscope (TEM) operating at 300 kV. The surface microstructure of the fabricated carbon films was checked on a FESEM (Supra 35VP, Carl Zeiss). BET specific surface area measurement and BJH pore size distribution analysis was performed using the Quantachrome (iQ3) instrument after evacuation at 80°C for 2h.

Similar BSO nanoparticles were used as reported in our previous report. [32, 33] The TiO_2 paste (18 NR-T and 18 NR-O) was obtained from Dyesol(R), now known as Greatcell Solar. Ruthenium 535 bis-TBA (N719) dye, Pt electrode, and plastic spacer (Meltonix) were obtained from Solaronix, SA in this work. The prepared I^-/I_3 electrolyte has been used for device testing. The complete assembling and final device fabrication protocol of the DSSC testing have been described in our previous report. [32] The active area of the dye-coated BSO and TiO_2 film was 0.2826 cm^2. Noteworthy, for TiO_2, the N719 dye-loading period was 24 h, whereas, only 20 min was the optimized dye dipping time in the case of BSO. [32] Besides, both the photoanodes has been tested with Pt and CZTS CEs, individually. Further, the photovoltaic performance of CZTS CEs was accomplished using the Wacom AAA continuous solar simulator (model: WXS-210S-20, AM1.5G). PCE of various devices, as mentioned in Figure 7 was measured using the mentioned solar simulator. The cyclic voltammetry and electrochemical impedance spectroscopy analysis were executed using the NOVA software equipped with the Autolab potentiostat/galvanostat instrument.

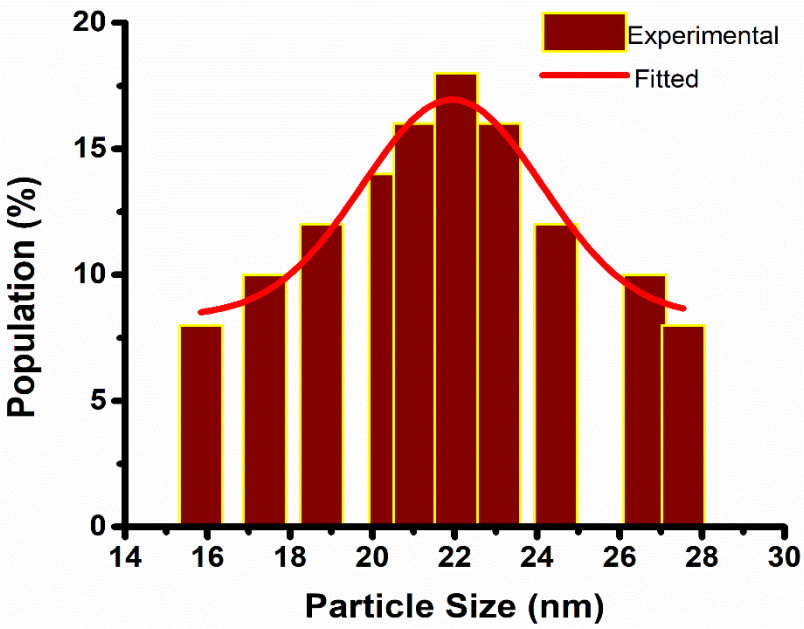

Figure S2. Particle size histogram plot of CZTS nanoparticles, as obtained by the TEM analysis.

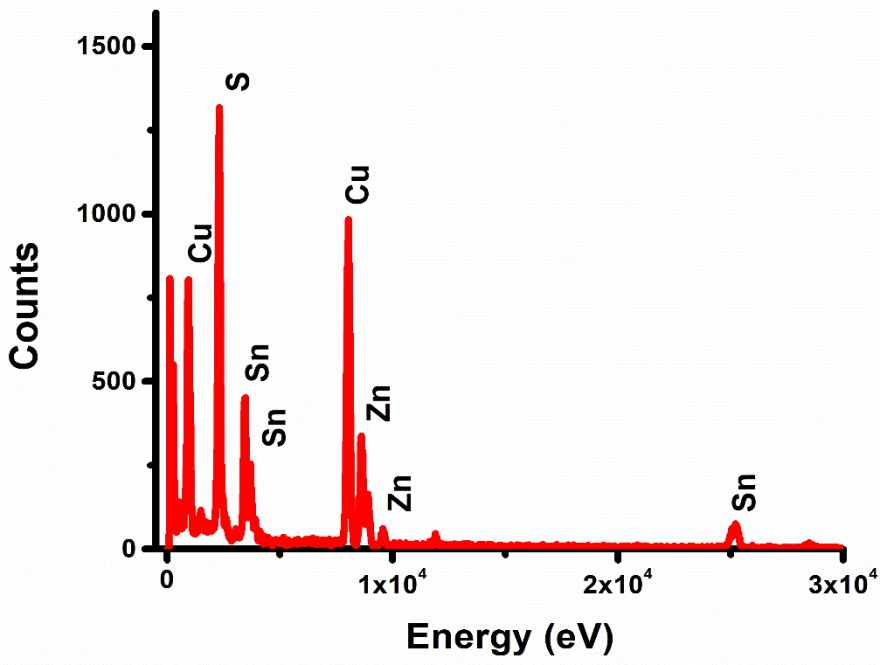

Figure S3. EDX plot of CZTS nanoparticles, as obtained by the TEM analysis.

\

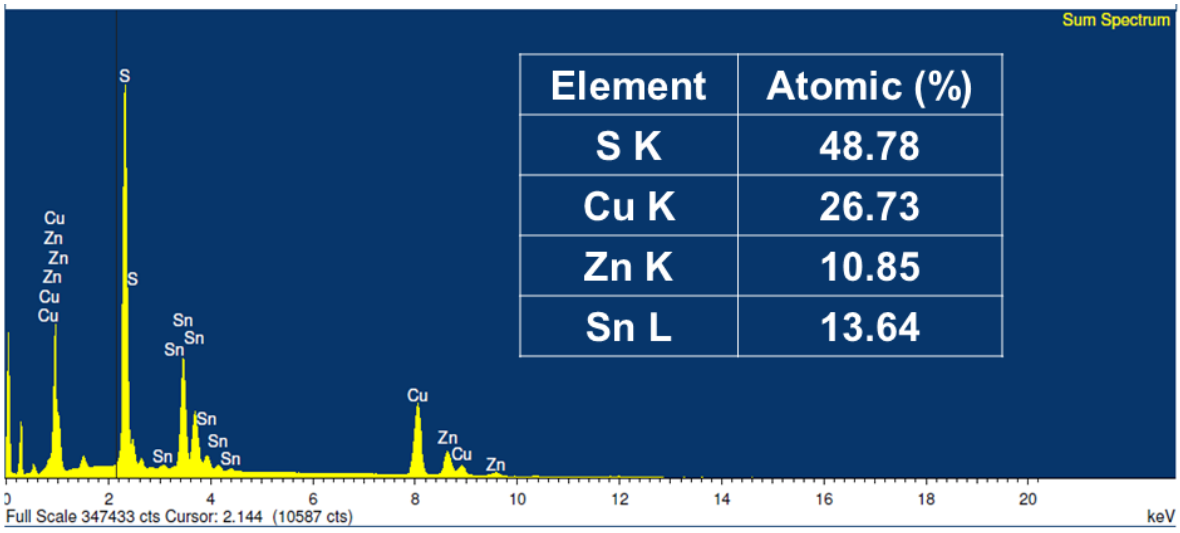

Figure S4. Quantitative EDX spectrum of CZTS thin film.

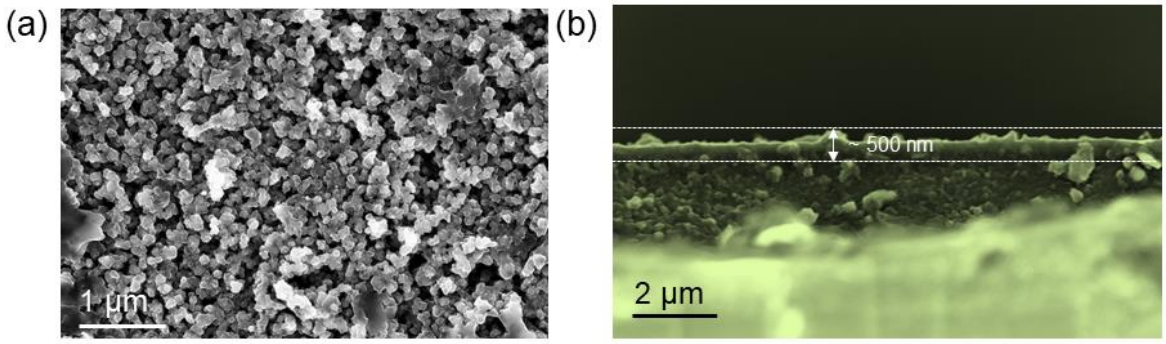

Figure S5. FESEM microstructural (a) top-view and (b) cross-sectional view images of the hydrothermally grown CZTS film on FTO glass.

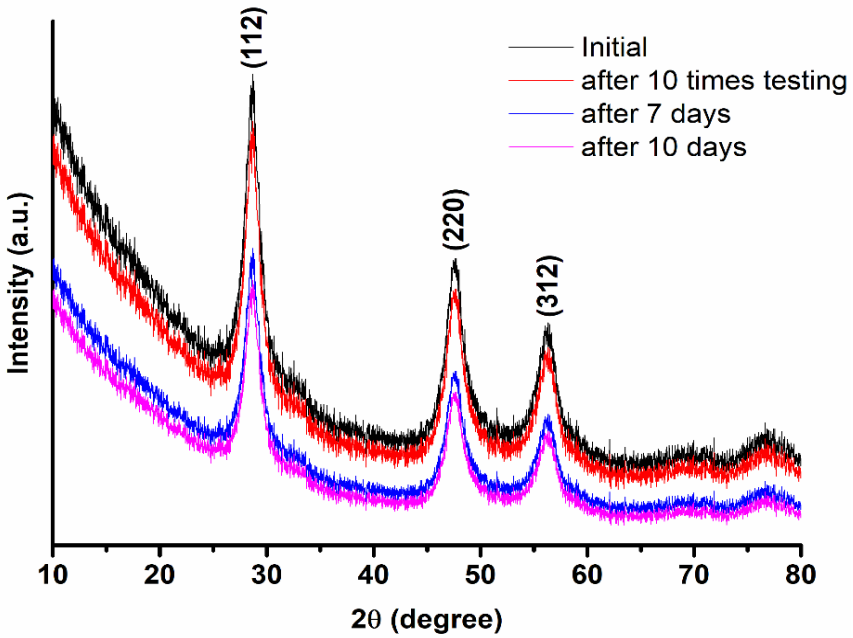

Figure S6. XRD pattern of CZTS thin film for the different set of period.